Copyright © 2011 by ABCM

VERTICAL COOLING ARRANGEMENT FOR ELECTROMAGNETIC LAUNCHERS

H. Zhao, zhao@caps.fsu.edu
J.A. Souza, souza@caps.fsu.edu
J.C. Ordonez, ordonez@caps.fsu.edu
Department of Mechanical Engineering and Center for Advanced Power Systems, Florida State University, Tallahassee, FL 32310

Abstract. *A three-dimensional transient electromagnetic and thermal analysis has been performed on an electromagnetic launcher (EML) with a moving armature. Coupled electromagnetic, thermal, and mechanical equations are solved to capture current distributions, temperature response in the rails and projectile launch velocity. The thermal management of EMLs becomes more important in applications in which multiple shots are required. In this study we consider the first shot in a sequence of shots occurring every 5 seconds with the actual launch lasting only 3 milliseconds. This paper studies the effects of introducing a vertical cooling channels arrangement after the determination of the temperature field during the launch process. The temperature distributions at the end of the 5s cooling period are compared for three different channel configurations. A no-cooling situation is also included for comparison. These comparisons can provide some directions to optimize thermal management of the EML rail conductor.*

Keywords*:* EML, electromagnetic analysis, thermal analysis, vertical cooling

1. INTRODUCTION

Electromagnetic launchers (EMLs) accelerate an object by electromagnetic forces along a guide-way to initiate subsequent flight. EMLs have the ability to achieve higher muzzle velocities than traditional propellant based launchers, have a long range of more than 300km, estimated lower costs per launch, and a reduced potential risk of explosion.

Figure 1 illustrates schematically an electromagnetic launcher. It consists of two rails along which an armature can move. Current circulates through the rails and armature inducing an electromagnetic field and a Lorentz force. The Lorentz force accelerates the armature which carries the projectile. The current circulated is typically very large resulting in large amounts of ohmic heat.

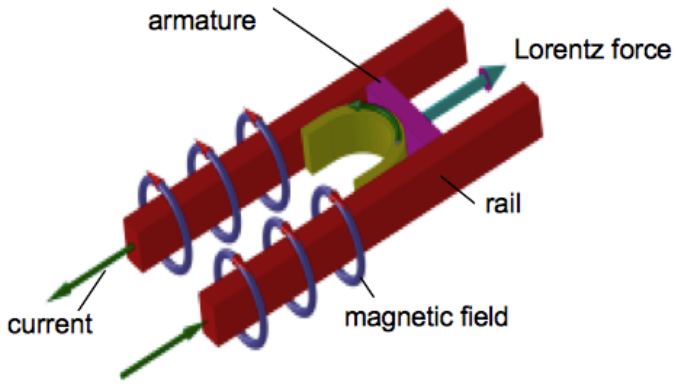

Figure 1. Schematic representation of an electromagnetic launcher

Among all the challenging technical issues, an effective thermal management for the rail conductors is crucial to the large scale EML designs especially when it is working in multi-shots mode. The internal cooling is an easily achievable way to complete the task. In the last twenty years, 2-D and 3-D studies have been conducted in this area (Kerrisk, 1986; Liu and Lewis, 1991; Jamison *et al.*, 1995; Fish, Phipps and Tang, 1999; Smith *et al.*, 2005). These studies were all analytical and numerical. None of these studies considered vertical cooling channels, that is, channels that are perpendicular to the main direction of the current flow. Some correlations, such as correlations between the firing rates and the coolant flow parameters, and the channel locations and the energy removal efficiency, were established. Also,

qualitative characteristics of the heat removal process were described, for instance, Liu (1991) found that heat reversal could occur in the rear part of the channels due to the high temperature gradient in the length direction.

In this paper, we study vertical cooling channels. The analysis is divided in two stages: 1) the launch process simulation (lasting only a few milliseconds) and 2) the cooling process before a subsequent shot (which last ~ 5s). In the first stage, the coupled electromagnetic, thermal and mechanical equations were solved to determine the temperature field. In the second stage, the fluid flow and heat transfer problems are solved to quantify the effect of the channels. Three different cooling channel distributions are considered and compared.

2. ELECTROMAGNETIC AND THERMAL MODELS

2.1. COMPUTATIONAL MODEL

A simple graphic representation of the EML computational domain is shown in Fig. 2, in which the two long black blocks represent the two rails. The thin block in between them is the movable armature. The outside cylinder represents the surrounding air, which is included to account for the surrounding magnetic fields. During the launching period, the current flows in through one rail; passes the armature, and flows back through the other rail. Due to the two symmetry planes in this configuration (Heish, 1995) only a quarter (top-right quarter included in the red edges) of the whole geometry is modeled in the present simulation.

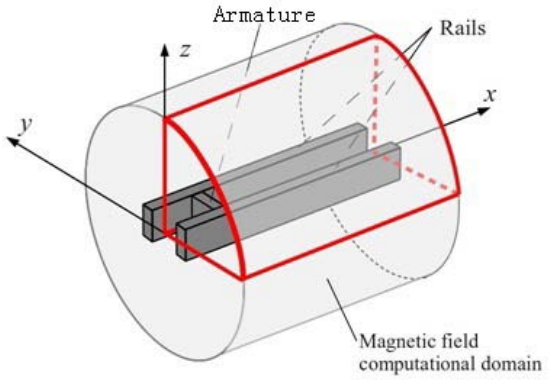

Figure 2. Computational domain used in the study of the EML

The projections of the top view and front view are shown in Fig. 3 together with the dimensions of the rails and the armature. The dimensions of the rail and the armature are selected to be 1.2m×0.06m×0.135m (x, y and z coordinate) and 0.2m×0.135m×0.135m, respectively. The surrounding air cylinder has the radius of 1m and has the same length of the rail.

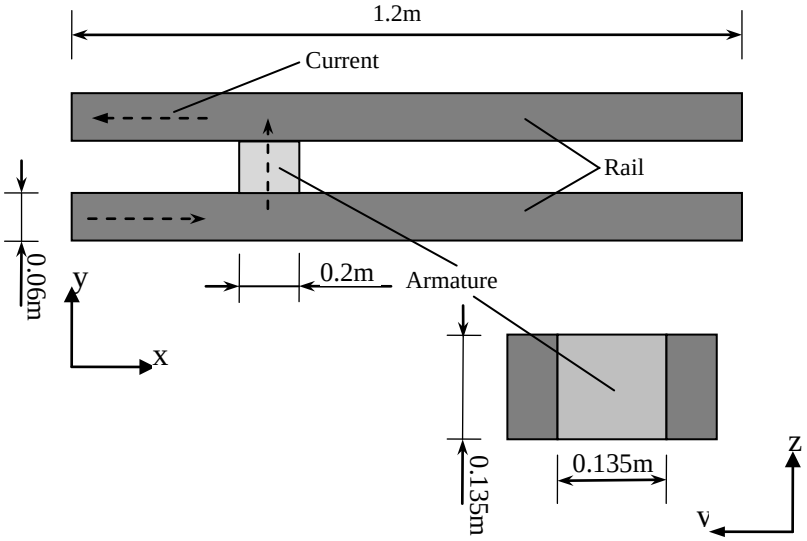

Figure 3. Rail projection views and current flow path (not in scale)

2.2. Governing Equations

The basic governing equations for the electromagnetic and thermal analyses are listed in Eqs. (1)–(3). The armature's motion is calculated by Eq. (4), where $\vec{A}$, V, T, x_a are the magnetic vector potential, the electric scalar potential, the temperature and the armature's position, respectively. These equations were developed from the Maxwell equations, energy equation and the Newton's second law (Zhao, Souza and Ordonez, 2008). The coefficients σ, μ_0, ρ, c_p, k, m, F_x are the electric conductivity, the electric permeability of free space, the density, specific heat, thermal conductivity, the mass of the armature and the projectile, and the Lorentz force in the armature's moving direction, respectively (Ulab, 2001; Incropera and Dewitt, 2001). In this study, the materials chosen for the rails and the armature are copper and aluminum, respectively. The mass of the armature and projectile combined is 20kg. In the development of these equations, the rigid armature and ideal contact on armature/rail interface have been assumed. Two aspects contribute to the coupling of the electromagnetic and thermal problems: i) among the coefficients, the properties of copper are treated as temperature dependent (while all others are treated as temperature independent) and ii) the current density results in the heat generation term in the energy equation.

In Eq. (3), the current has the expression $\vec{J} = \sigma(-\nabla V - \frac{\partial \vec{A}}{\partial t})$. Through the electric conductivity and the current, the first three equations are coupled together. After solving the first three governing equations for the current time step, the Lorentz force can be integrated and then the armature's position for the next time step can be found.

$$\sigma \frac{\partial \vec{A}}{\partial t} + \frac{1}{\mu_0}(\nabla \times (\nabla \times \vec{A})) + \sigma \nabla V = 0 \tag{1}$$

$$\nabla \cdot (\sigma \nabla V) = 0 \tag{2}$$

$$\rho c_p \frac{\partial T}{\partial t} = \nabla \cdot (k \nabla T) + \frac{\vec{J} \cdot \vec{J}}{\sigma} \tag{3}$$

$$m \frac{d^2 x_a}{dt^2} = F_x \tag{4}$$

2.3. Boundary and Initial Conditions

For the magnetic vector potential in Eq. (1) a "magnetic insulation" boundary condition (Eq. (5)) is applied to the boundaries confining the outside surrounding air (surfaces 1, 2, and 3 in Fig. 3), the symmetry plane where the magnetic field is known to be tangential to it (Cheng, 1989) (surfaces 5 and 9), and the surfaces which are the interfaces between the conductor and the air (surfaces 6 and 7). For the other symmetry plane – the horizontal symmetry plane (surfaces 4 and 8), an "electric insulation" boundary condition (Eq. (6)) is applied.

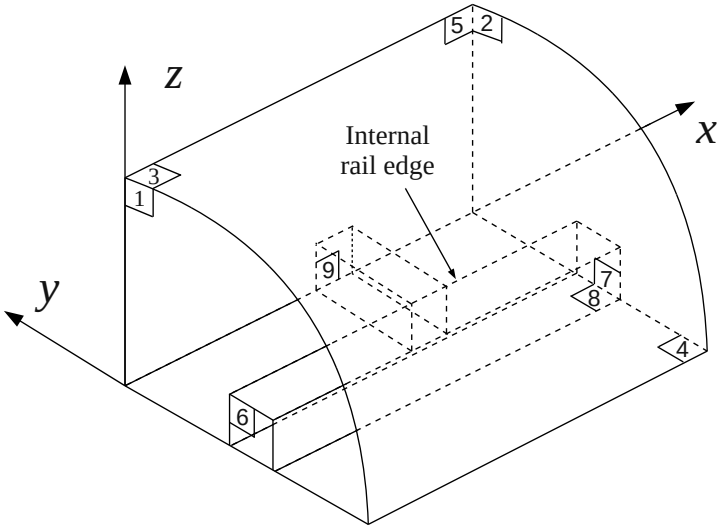

Figure 4. Boundary indexes

For the electric scalar potential (Eq. (2)), a prescribed voltage (Eq. (7)) is applied to the current inlet boundary (surface 6 in Fig. 4). Ground condition (Eq. 8) is applied to the current outlet boundary (surface 9), i.e. the armature symmetry boundary. For all the other boundaries the condition "current insulation" (Eq. 9) is applied. In the boundary conditions, the vector $\vec{n}$ represents the outward normal direction vector.

$$\vec{n} \times \vec{A} = 0 \tag{5}$$

$$\vec{n} \times \vec{H} = 0 \tag{6}$$

$$V = V(t) \tag{7}$$

$$V = 0 \tag{8}$$

$$\vec{n} \times \vec{J} = 0 \tag{9}$$

$$\vec{n} \cdot \nabla T = 0 \tag{10}$$

The adiabatic condition (Eq. (10)) is applied to all the rail boundary faces. In this way, by neglecting the heat convection on the rail exterior boundaries, the worst case situation in the short launch period (~3ms) is considered.

Initially, there is no magnetic field ($\vec{A} = 0$) and no current (V=0 everywhere). The armature is located at x_a=0.2m and the initial rail temperature is 293.15 K. After setting the boundary conditions and initial conditions, the problem given by Eqs. (1)-(10) was solved using a finite element solver (COMSOL, 2005).

2.4. Simulation Results

The chosen voltage potential and the calculated inlet current are shown in Fig. 5. Because only half of one rail is modeled in the simulation, the current value shown in this figure is only half of the total inlet current.

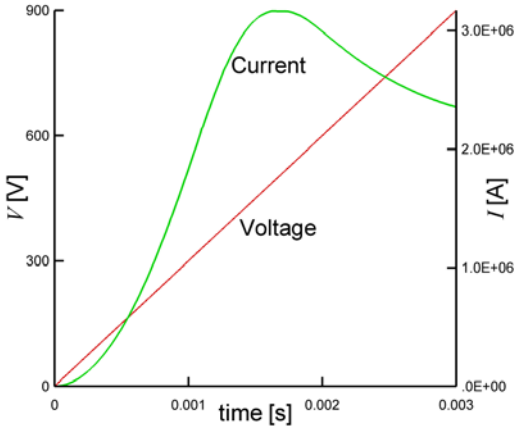

Figure 5. Voltage and inlet current

The temperature response of the half of the rail after the shot is given in Fig. 6. Due to the skin effect, the current concentrates on the internal edges (edges on the internal faces, see Fig. 4) and the internal surfaces. So in the whole rail, the temperature profile is highly non-uniform.

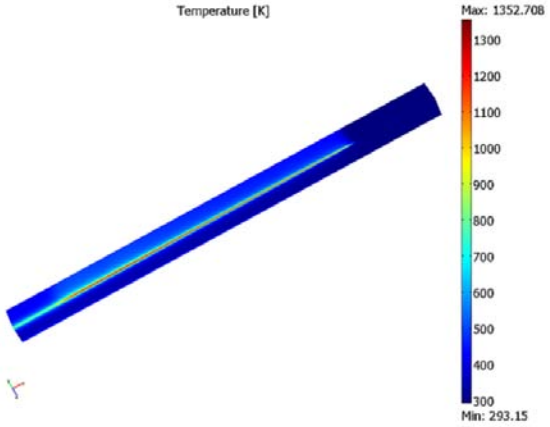

Figure 6. Temperature response after the shot

To clearly show this feature, the temperature profiles on the rail cross-section on which the maximum temperature occurs (x=0.315m) and on the internal edge are shown in Fig.7. Figure 7a clearly shows the highly non-uniform temperature distribution on the cross section. Most of the internal area is still at the initial temperature after the first shot. Figure 7b shows the other non-uniform feature along the rail length direction. Along the positive length direction, the temperature increases quickly from the inlet, reaches its maximum value at x=0.315m, decrease at a relatively low rate until x=1.0m, then falls to the initial value. The 0.2m-long end area was still at the initial temperature because at end of the current pulse the armature did not reach that region.

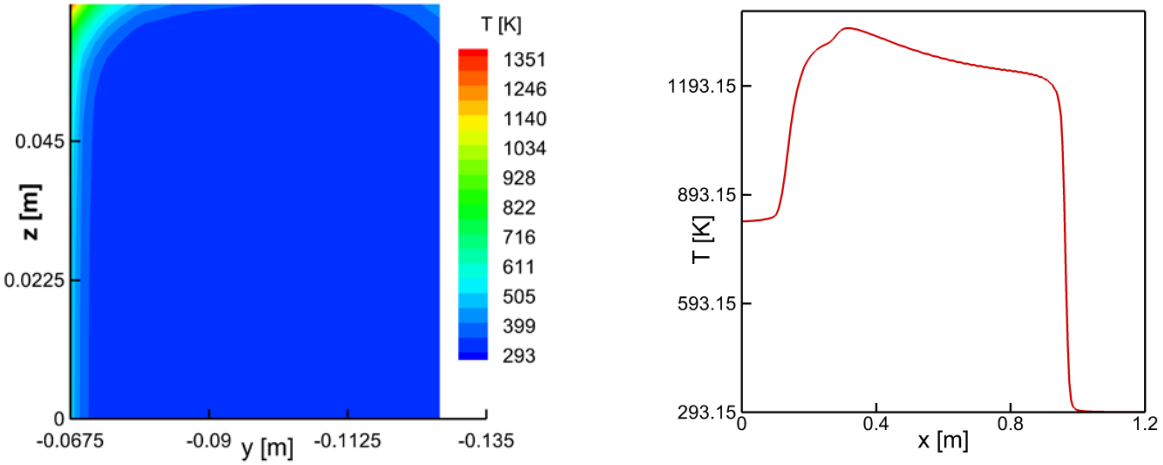

a. Half cross section temperature at x=0.315m at t=3ms

b. Internal edge (see Fig. 3) temperature (t= 3ms)

Figure 7. Temperature distribution after the shot

3. Thermal Management

EML thermal management should include the identification of the temperatures and cooling schemes that maximize the launcher performance. In this study we limit the scope to the identification of temperature field and the effects that different cooling arrangements have on it. We study a "no-cooling" situation, in which no channels are present, and situations with eight vertical channels placed throughout the length of the rail with different channel-to-channel spacing.

3.1. No-cooling investigation

The temperature distribution shown in Fig. 7a, after the first shot (t=3ms) corresponds to solve the heat conduction equation (Eq.(11)). During the cooling period, 3ms < t < 5 s, it was assumed that no further current circulates throught the rails and then, no source term appears in the heat conduction equation. The problem is essentially one of heat diffusion resulting from a non-uniform initial temperature distribution. From Fig. 7a, it is possible to observe that the core of the rail is still at a low temperature and serves as a heat sink. This heat sink is very effective in reducing the rail peak temperature, due to the high thermal conductivity of copper and the large temperature gradients driving the heat fluxes.

$$\rho c_p \frac{\partial T}{\partial t} = \nabla \cdot (k \nabla T) \tag{11}$$

Because the temperature field will also be symmetric about the middle *x*-*y* plane in the cooling period (which is not the case for the following vertical cooling analyses), half of one rail was kept to be our computational domain. Adiabatic boundary conditions were assigned to all boundary surfaces to consider the worst-case condition. Due to this boundary condition's restriction, in the no-cooling case, all the deposited heat will remain in the rail.

According to the desired design parameters, the anticipated firing rate is 12 rounds per minute. It results in a 5s cooling period between two shots. The temperature profile on the internal edge before and after the 5s cooling period is shown in Fig. 8. At *t*=3ms, the maximum temperature is higher than 1300K. After 5s, the maximum temperature drops to less than 340K due to the high thermal conductivity of copper and the existence of the low-temperature region. Another point that should be noticed is that the maximum temperature's position shifted from *x*=0.3m to *x*=0.15m.

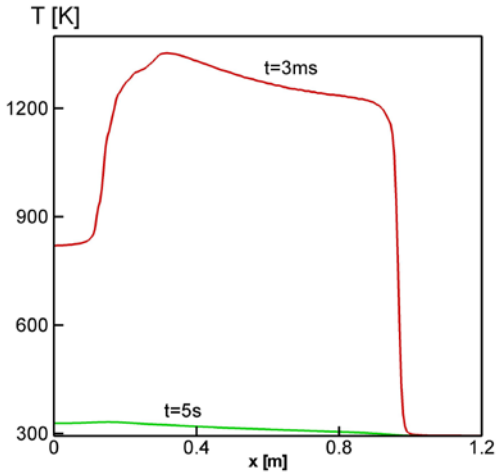

Figure 8. Internal edge temperature for no-cooling case

3.2. Vertical cooling investigation

3.2.1. Channel distribution

As mentioned in the introduction, there have been studies considering the thermal management of EMLs using cooling channels along the rail length direction. But for a long rail with high temperature gradient along the length direction, heat reversal can occur on the downstream (Liu, 1991). To avoid the heat reversal, an alternative cooling scheme, the vertical cooling, is investigated here (Fig. 9). The number of cooling channels was fixed to 8 and the diameters for all channels were chosen to be 0.012m. In the vertical cooling configuration, the temperature field will no longer be symmetric about the middle x-y (horizontal plane in Fig. 9) plane. So the whole rail needs to be included in the computational domain.

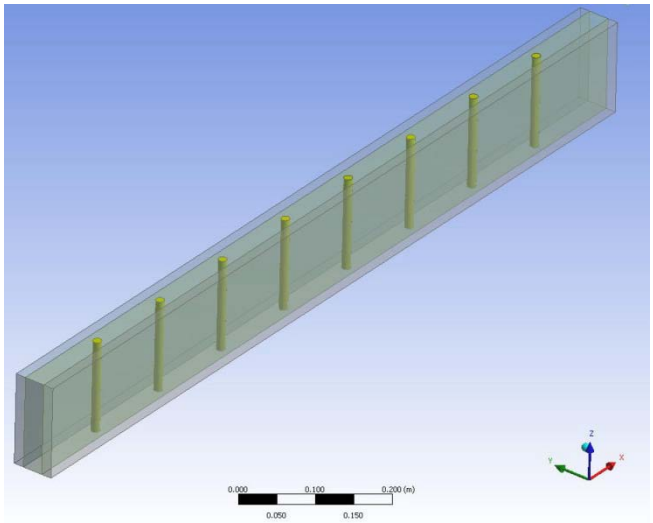

Figure. 9 Layout of vertical cooling channels

Three different channel distributions were studied to evaluate the impact of the distribution on the cooling effectiveness. The relative position of the channels in the x-direction was selected using MATLAB (The MathWorks, 2008) function Geospace (x_0, x_N, N, G). This function generates N points between x_1 and x_N with a spacing that is G times bigger than the previous step. In the y-direction (rail width), all channels are located on the middle plane. The parameters used in these three cases are listed in table 1. The case 1 is a uniform distribution with the first channel located on x_0=0.1333m. In case 2 and case 3, the first channel was kept on the same location, whereas the following channels took the different distribution by changing the G value. Larger G-values result in the channels being more concentrated towards the front part of the rail.

Table 1. Channel distribution parameters

	G	X_1	x_2	x_3	x_4	x_5	x_6	x_7	x_8
1	1	0.1333	0.2667	0.4	0.5333	0.6667	0.8	0.9333	1.0667
2	1.3	0.1333	0.1780	0.2361	0.3117	0.4099	0.5376	0.7036	0.9194
3	1.5	0.1333	0.1550	0.1874	0.2362	0.3093	0.4189	0.5833	0.8300

3.2.2. Governing equations

The coolant is water and the flow direction is positive z-axis. A preselected mean velocity w = 2m/s was applied to all channel inlets. By substituting the parameters into Eq. (12), the calculated Reynolds number is 2.1×10^4. So the incompressible turbulent flow was assumed for all following cases. The physical properties of water were all taken as constants: ρ_w=998.2kg/m^3, c_{pw}=4182$J/(kg{\cdot}K)$, k_w=0.6W/(m·K), and μ=0.001003$kg/(m{\cdot}s)$.

$$\mathrm{Re}_D = \frac{\overline{u}_{ave} D}{\nu} \tag{12}$$

The Reynolds-averaged Navier-Stokes (RANS) equations for incompressible flows are Eqs. (12) and (13):

$$\nabla \cdot U = 0 \tag{13}$$

$$\rho_w \frac{\partial U}{\partial t} + \rho_w U \cdot \nabla U + \rho_w \nabla \cdot \overline{(u' \otimes u')} = -\nabla P + \nabla \cdot [\mu(\nabla U + (\nabla U)^T)] \tag{14}$$

where $\boldsymbol{U}$ is the average velocity field; $\otimes$ is the outer vector product; P is the pressure. The third term in the left hand side of Eq. (14) is the Reynolds stress tensor. The Reynolds stress can be expressed in Eq. (15):

$$\rho_w \nabla \cdot \overline{(u' \otimes u')} = -\mu_t (\nabla U + (\nabla U)^T) + \frac{2}{3}\rho_w k_t \tag{15}$$

where k_t is the turbulence kinetic energy; μ_t is the turbulent viscosity. The standard k-ε model was used to determine the k_t and μ_t.

The energy equation inside the cooling channels is as in Eq. (16):

$$\rho_w c_{pw} \frac{\partial T}{\partial t} + \rho_w c_{pw} U \cdot \nabla T = \nabla \left[\left(k_w + \frac{c_{pw}\mu_t}{\mathrm{Pr}\, t} \right) \nabla T \right] \tag{16}$$

where *Prt* is the turbulent Prandtl number.

For the solid part, the governing equation is the same as in Eq. (11). The software package FLUENT (ANSYS, 2009) was used to perform the cooling analysis.

3.2.3. Boundary conditions

All the 8 channels had the same boundary conditions. For the fluid flow, a prescribed velocity of 2m/s was imposed at the channel inlet, at the outlets the flow was assumed fully developed. The no-slip condition was applied on the channel walls. For the energy equation, the prescribed temperature T=293.15K was set at the channel inlet, and a zero temperature gradient was imposed at the channel outlet. On the channel walls, the advective heat flux in the fluid was set to be equal to the conductive heat flux in the solid. For all the other solid surfaces, the adiabatic condition was applied.

3.2.4. Initial conditions

In the launch simulation, the rail is solid. No channels are included in the rails. From the cross section temperature profile Fig. 7a, most of the inner regions are still at the initial temperature because the current skin effect makes the current concentrate on the edges and surfaces. This temperature distribution during the early regime (t < 3ms), suggest that the inclusion of channels towards the core (away from the skin) will not affect the initial temperature field. This feature allows us to make the simplifying assumption that the temperature of the solid rail after the launch process can be used as the common initial temperature field for cases with or without channels. This simplification considerably reduces the computational time, since the launch process needs to be computed only once.

Unlike the no-cooling case, in the vertical cooling configuration, the temperature field is not symmetric about the middle *x-y* plane and the computational domain must be extended to the whole rail (see Fig.9). The initial temperature field for the lower half rail was set by the symmetric condition about the middle *x-y* plane (valid in the launch process). For the coolant, the initial temperature is set to be 293.15K.

3.2.5. Results and discussions

Case 1 in Table 1 corresponds to an even distribution of 8 channels. The temperature field after 5s' cooling period is shown in Fig. 10. From this figure, it is clear that each channel can control the adjacent temperature.

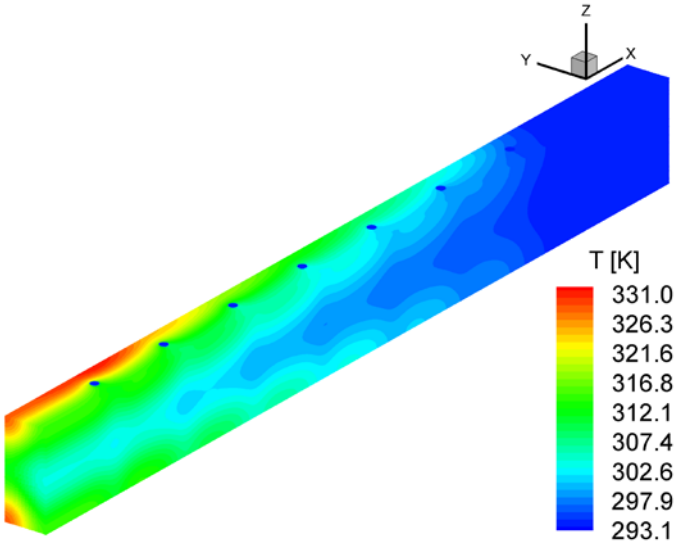

Figure 10. Temperature field for case1 at t=5s

The hotter internal edge temperature is shown in Fig. 11 together with the no-cooling case. As was mentioned in previous section, the temperature field is no longer symmetric about the middle *x-y* plane. So the two internal edges had different temperature profiles. The internal edge on the top surface had a higher temperature than the one on the bottom surface. In Fig.11, the hotter internal edge represents the edge on the top surface.

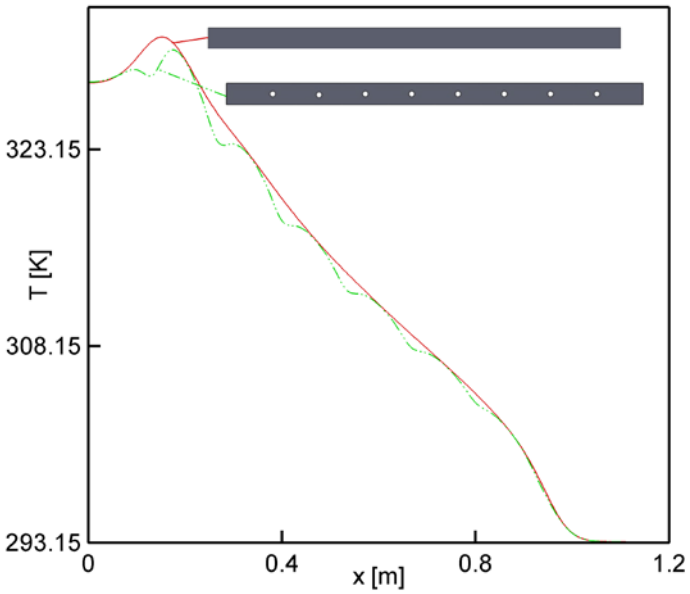

Figure 11. Internal edge temperature profile

The temperature in the regions next to the cooling channels are significantly reduced, however for regions away from the channels, the temperature shows not much difference from the no-cooling case. The channels are more effective in reducing the temperature in the hotter regions (towards x =0), while the channels towards the rail end (x =1.2) (channels 7th and 8th) produce very small temperature drops when compared to the no-cooling situation.

The hotter internal edge temperature for all the three cases at t=5s is shown in Fig. 12. As expected, the concentration of channels towards the higher temperature region lowers the maximum temperature. Nevertheless, the high concentration of channels in higher temperature region will cause less channels in the lower temperature region, and thus in some regions the cases 2 and 3 will have a higher temperature than the case 1. However, the goal in this work is to control the maximum temperature to protect the rail from melting and in this respect the uneven channel distribution is beneficial.

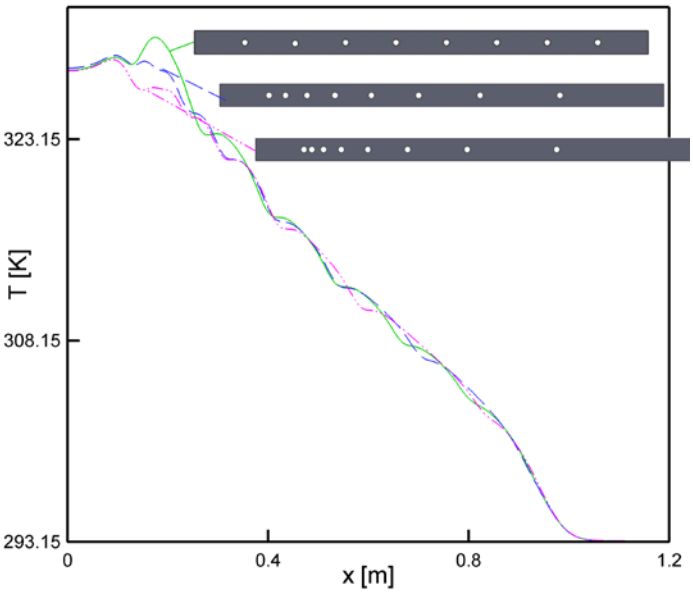

Figure 12. Internal edge temperature profile for three cooling cases

The temperature profile at x=0.1333m, t = 5s (center plane of the first channel) for the case 1 is shown in Fig. 13. The water inside the channel has lower temperature than the solid. The heat reversal is avoided as we expected.

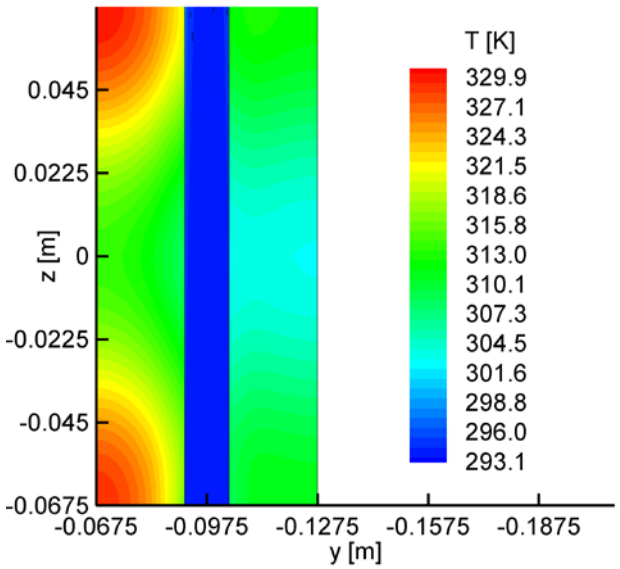

Figure 13. Temperature profile of the center-plane for the first channel of case 1

4. Conclusions

In this paper a model for an electromagnetic launcher is presented. The model allows for the computation of current and temperature distribution in the rails of the EML as well as the projectile launch velocity. Two stages are considered: the launch (early stage),which lasts only a few milliseconds, and the cooling stage that occurs in a period of 5 seconds and finishes when the subsequent shot starts. The model is solved using a combined finite element/ finite volume approach implemented in COMSOL and ANSYS.

By studying a case with no cooling channels it was established that the core section of the rail does not feel the energy deposited in it during the duration of the launching process (3 ms). This observation allowed for the introduction of the simplifying assumption of common initial temperature distribution (at t=3ms) for rails with and without cooling channels to study the cooling phase.

By examining three vertical cooling cases and the no-cooling case, it was found that the vertical cooling scheme avoids heat reversal, and it is effective controlling the maximum rail temperature. Additionally, the effectiveness of the vertical cooling scheme was higher when the channels were concentrated in the high temperature region.

In this first study, the coolant flow rate was selected a priori, and the results indicate (Fig. 13) that most of the coolant is still at the inlet temperature when reaching the outlet section. This suggests that the chosen flow rate is large and that the optimal flow rate should be determined in a follow up study.

5. Acknowledgements

The authors acknowledge with gratitude support from the Office of Naval Research (ONR)

6. References

ANSYS FLUENT 12, theory guide, ANSYS, Inc., 2009.

Cheng, D. K., Field and Wave Electromagnetics, Addison-Wesley, 2nd edition, 1989.

COMSOL Multiphysics Inc., user's manual, Los Angeles, CA, 2005.

Fish, S., Phipps, C., and Tang, V., 1999, "Rail heating analysis for multishot EM gun operation," IEEE transactions on magnetics, Vol. 35, No. 1, pp. 398-402.

Hsieh, K. T., 1995, "A Lagrangian formulation for mechanically, thermally coupled electromagnetic diffusive processes with moving conductors," IEEE transactions on magnetic, Vol. 31, No. 1, pp 604-609.

Incropera, F. P.and Dewitt, D. P., Fundamentals of Heat and Mass Transfer, Wiley, Fifth edition, 2001.

Jamison K. A., *et al.*, 1995, "Thermal loading and heat removal from a sequentially fired railgun," IEEE transactions on magnetics, Vol. 31, No. 1, pp. 314-319.

Kerrisk, J. F., "Railgun conductor heating from multiple current pulses," 1986, IEEE transactions on magnetics, Vol. 22, No. 6, pp. 1561-1566.

Liu, H. P., and Lewis, M. C., 1991, "3-Dimensional rail cooling analysis for a repetitively fired railgun," IEEE transactions on magnetics, Vol. 27, pp. 68-73.

MATLAB R2008a, The MathWorks, Inc.

Smith, A. N., *et al.*, 2005, "Thermal management and resistive rail heating of a large-scale Naval electromagnetic launcher," IEEE transactions on magnetics, vol. 41, No. 1, pp. 235-240.

Ulab, F. T., Fundamentals of Applied Electromagnetics, Prentice Hall, 2001 Media edition.

Zhao, H., Souza, J. A., and Ordonez, J. C., 2008, "Thermal model for electromagnetic launchers," Thermal Engineering, Vol. 7, pp. 59-64.